# Integral method for echelles covered with lossless or absorbing thin dielectric layers

Evgeny Popov, Bozhan Bozhkov, Daniel Maystre, and John Hoose

We make a generalization of the integral method in the electromagnetic theory of gratings to study diffraction by echelles covered with dielectric lossless or absorbing layers. Numerical examples are given that show that, as in the resonance domain, the diffraction efficiency is more complicated than being a simple product of lossless diffraction efficiency curves and plane surface reflectivity. 

*OCIS codes:* 050.1950, 050.1960.

## 1. Introduction

There has been much activity recently directed to improving and generalizing rigorous methods for modeling light diffraction by relief gratings. The differential method[1] was combined with the *s*-matrix algorithm[2] to improve the stability of the algorithm for modeling highly conducting metallic gratings in TM polarization.[3] The rigorous coupled-wave approach proposed by Moharam and Gaylord[4] was improved in a similar manner,[5] and recently its convergence in the TM case became as fast as in the TE case.[6,7] The method of coordinate transformations proposed by Chandezon *et al.*[8] was extended to gratings with vertical facets[9] and to gratings made from inhomogeneous materials.[10]

However, there is a grating problem that combines several difficulties that make it incapable of being treated by any of these theoretical methods (at least, there is no sign in the literature that one of these methods would be efficacious). The problem is the diffraction of light by reflecting echelles, in which (i) the wavelength $\lambda$ is much shorter than the period $d$ (i.e., there are many propagating orders), (ii) the incidence is at high angles, (iii) the high efficiency is in orders of high number, typically 100 or more, and (iv) the grating material is typically aluminum with high reflectivity. The small $\lambda/d$ ratio causes a further inconvenience in modeling, in as much as the grating profile must be represented quite closely to reality, because slight variations lead to significant changes in the efficiency of distribution between diffraction orders. Any stepwiselike or Fourier representation of the profile will require thousands of steps or harmonics, which explains the failure of the numerical methods mentioned above.

The only solution to the problem that has proved reliable so far is the integral method,[11] improved to encompass the integration variable as the curvilinear coordinate along the profile. In addition, special care is taken in treating the edges of the profile by increasing the density of the integration points about them. As a result, it has become possible to study diffraction by echelles, and a comparison with experimental results[12] confirmed the validity of the method, which is capable of dealing with diffraction in very high orders [as many as to 660 (Ref. 13)] as well as in low and intermediate orders.

However, echelles are also used in the spectral interval where the influence of aluminium oxide naturally formed upon the surface becomes nonnegligible. Moreover, the absorption of $Al_2O_3$ leads to a drastic reduction of reflectivity (and thus of efficiency) below 150-nm wavelength, which requires special coatings to move the absorption edge to shorter wavelengths. There are several formulations of the integral method to deal with gratings covered with one or several dielectric layers,[14–16] independently of their thickness. However, they all (or at least the numerical code proposed) use a

E. Popov (popov@mBox.cit.bg) and B. Bozhkov are with the Institute of Solid State Physics, 72 Tzarigradsko Chaussee, 1784 Sofia, Bulgaria. D. Maystre is with the Laboratoire d'Optique Electromagnétique, Case 262, Faculté des Sciences et Techniques de Saint Jérôme, Avenue Escadrille Normandie-Niemen, 13397 Marseille Cedex 20, France. J. Hoose is with Spectronic Instruments, Inc., 820 Linden Avenue, Rochester, New York 14625.

Received 12 May 1998; revised manuscript received 9 September 1998.

0003-6935/99/010047-09$15.00/0

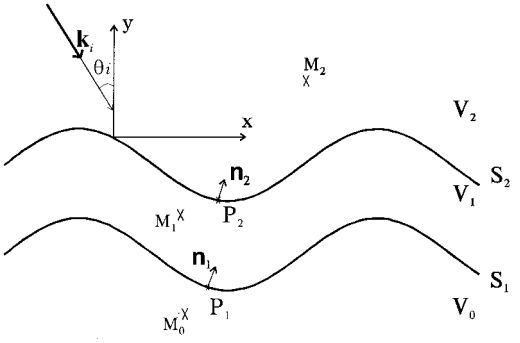


Fig. 1. Schematic representation of a grating covered by a dielectric layer, together with the notation used in the text.

Fourier representation of the profile, smooth profiles without edges, or both. The only numerical realization specially made to deal with echelles, as explained above, could not make possible the modeling of the influence of thin coatings on deep gratings. The reason is that the connection between the field values evaluated on the two closely situated profile surfaces was done by use of the *s*-matrix method,[17] which requires that a homogeneous region exist between profiles in which the field can be represented in a Rayleigh expansion.[18] For example, when there is no interpenetration of the profiles, in the region between the groove top of the lower profile and the groove bottom of the upper profile Rayleigh expansion is valid. However, it is not valid inside the grooves of deep gratings or for profiles with edges[19]; thus, when such profiles interpenetrate, such a homogeneous region does not exist between them. Numerical methods based on the Rayleigh hypothesis proved to be valid for much deeper gratings [groove depth-to-period ratio $h/d$ as great as 6 (Ref. 20)] than were theoretically predicted ($h/d$ as much as 0.142 for a sinusoidal profile), but this works only for sinusoidal groove forms[21] and only in the far-field zone, resulting in a large error in the near-field zone.[22] This is why for echelles covered with thin dielectric layers it is necessary to consider coupled integral equations for the field components evaluated on the different profiles and to be able to solve them simultaneously. Here we present details of this procedure, together with several numerical examples.

### 2. Integral Method as Applied to a Layered Grating

Let us consider a diffraction grating covered with a layer of dielectric material, which can be absorbing or not. The notation and the corresponding coordinate system are introduced in Fig. 1. The essence of the integral method lies in the fact that the field everywhere in space can be represented as an integral over the profile(s) of the components of the electromagnetic field that are tangential to these profiles, multiplied by the corresponding Green's functions.

Let $\psi$ denote the $z$ component of the electromagnetic field and $\phi$ be its normal derivative. In TE polarization $\psi$ stands for the $z$ component of the electric field $E_z$; in the TM case, for the $z$ component of the magnetic field $H_z$. As $\psi$ and $\phi$ are defined only on the profiles, they are identified by subscript 1 or 2, depending on for which profile they are defined. In the TM case with the magnetic-field vector parallel to the grooves in the $z$ direction its normal derivative is discontinuous at the profile because of the change in electric permittivity; in the TE case the normal derivative of the magnetic field has a jump if magnetic permittivities of the media differ. Thus $\phi$ can have different values at the two sides of the corresponding profile, and it is assigned a superscript + or −, indicating that $\phi$ is calculated on the upper ($\phi^+$) or lower ($\phi^-$) side of the profile surface. When we are dealing with the classical diffraction case with the plane of incidence perpendicular to the grooves there is no $z$ dependence.

$F$ represents the $z$ component of the electric (for the TE case) or the magnetic (for the TM case) field. It takes subscripts 0–2 in the regions $V_{0,1,2}$ in Fig. 1. We define functions $U$ in the following manner:

$$U_0 = \begin{cases} F_0 \exp(-i\alpha_0 x) & \text{in } V_0 \\ 0 & \text{elsewhere} \end{cases},$$

$$U_1 = \begin{cases} F_1 \exp(-i\alpha_0 x) & \text{in } V_1 \\ 0 & \text{elsewhere} \end{cases},$$

$$U_2 = \begin{cases} (F_2 - F_i)\exp(-i\alpha_0 x) & \text{in } V_2 \\ 0 & \text{elsewhere} \end{cases}, \tag{1}$$

where $F_i$ denotes the incident wave:

$$F_i(x, y) = \begin{cases} \exp\left(i\alpha_0 x - i\dfrac{2\pi}{\lambda}\nu_2 \cos\theta_i y\right) & \text{in } V_2 \\ 0 & \text{elsewhere} \end{cases}, \tag{2}$$

and $\alpha_0$ is the $x$ component of the incident wave vector $\mathbf{k}_i$:

$$\alpha_0 = \frac{2\pi}{\lambda}\nu_2 \sin\theta_i, \tag{3}$$

where $\lambda$ is the wavelength, $\nu_2$ is the refractive index of the upper medium, and $\theta_i$ is the angle of incidence.

Everywhere in the region below the lower profile $S_1$ the function $U_0(x, y)$ can be represented as an integral over this profile:

$$\text{Below } S_1: \qquad U_0(x, y) = -\int_{S_1} \mathcal{A}_1^-(x, y, s_1)\phi_1^-(s_1)\mathrm{d}s_1 - \int_{S_1} \mathcal{B}_1^-(x, y, s_1)\psi_1^-(s_1)\mathrm{d}s_1, \tag{4}$$

where $s_1$ is the curvilinear coordinate along the profile $S_1$ and Green's functions $\mathcal{A}$ and $\mathcal{B}$ are given in Eqs. (7) and (8). Between the two profiles, $U_1$ is

generated by the corresponding functions on the two profiles:

Between $S_1$ and $S_2$:

$$U_1(x,y) = \int_{S_1} \mathcal{A}_1^{+}(x,y,s_1)\phi_1^{+}(s_1)\mathrm{d}s_1 + \int_{S_1} \mathcal{B}_1^{+}(x,y,s_1)\psi_1^{+}(s_1)\mathrm{d}s_1 - \int_{S_2} \mathcal{A}_2^{-}(x,y,s_2)\phi_2^{-}(s_2)\mathrm{d}s_2 - \int_{S_2} \mathcal{B}_2^{-}(x,y,s_2)\psi_2^{-}(s_2)\mathrm{d}s_2. \quad (5)$$

The signs of the integrals result from the anticlockwise positive direction chosen for the contour integral, so the upper profile is run from right to left, i.e., in the negative direction of the coordinate $s_2$. In the same manner, in the upper region $U_2$ is derived by an integral along the upper profile, as far as the incident-field part is already deduced from it [Eqs. (1)]:

$$\text{Above } S_2: \quad U_2(x,y) = \int_{S_2} \mathcal{A}_2^{+}(x,y,s_2)\phi_2^{+}(s_2)\mathrm{d}s_2 + \int_{S_2} \mathcal{B}_2^{+}(x,y,s_2)\psi_2^{+}(s_2)\mathrm{d}s_2. \quad (6)$$

$\mathcal{A}$ and $\mathcal{B}$ are the Green's functions[11]:

$$\mathcal{A}_j^{\pm}(x,y,s_j) = \frac{1}{2id}\sum_{m=-\infty}^{\infty}\frac{1}{\beta_{j,m}^{\pm}}\exp\{\mathrm{Im}\,K[x - x_j(s_j)] + i\beta_{j,m}^{\pm}|y - y_j(s_j)|\}, \quad (7)$$

$$\mathcal{B}_j^{\pm}(x,y,s_j) = \frac{1}{2d}\sum_{m=-\infty}^{\infty}\left\{\frac{\mathrm{d}x_j}{\mathrm{d}s_j}\,\mathrm{sgn}[y - y_j(s_j)] - \frac{\alpha_m}{\beta_{j,m}^{\pm}}\frac{\mathrm{d}y_j}{\mathrm{d}s_j}\right\}\exp\{\mathrm{Im}\,K[x - x_j(s_j)] + i\beta_{j,m}^{\pm}|y - y_j(s_j)|\}, \quad (8)$$

where

$$\alpha_m = \alpha_0 + mK, \quad (9a)$$

$$K = \frac{2\pi}{d}, \quad (9b)$$

$$\beta_{1,m}^{-} = \left[\left(\frac{2\pi}{\lambda}\nu_0\right)^2 - \alpha_m^{\,2}\right]^{1/2}, \quad (9c)$$

$$\beta_{1,m}^{+} = \beta_{2,m}^{-} = \left[\left(\frac{2\pi}{\lambda}\nu_1\right)^2 - \alpha_m^{\,2}\right]^{1/2}, \quad (9d)$$

$$\beta_{2,m}^{+} = \left[\left(\frac{2\pi}{\lambda}\nu_2\right)^2 - \alpha_m^{\,2}\right]^{1/2}. \quad (9e)$$

According to the definitions,

$$\psi_1^{-} = F_0(s_1)\exp[-i\alpha_0 x(s_1)] \equiv \lim_{M_0\to P_1} U_0(x,y), \quad (10a)$$

$$\psi_1^{+} = F_1(s_1)\exp[-i\alpha_0 x(s_1)] \equiv \lim_{M_1\to P_1} U_1(x,y), \quad (10b)$$

$$\psi_2^{-} = F_1(s_2)\exp[-i\alpha_0 x(s_2)] \equiv \lim_{M_1\to P_2} U_1(x,y), \quad (10c)$$

$$\psi_2^{+} = [F_2(s_2) - F_i(s_2)]\exp[-i\alpha_0 x(s_2)] \equiv \lim_{M_2\to P_2} U_2(x,y), \quad (10d)$$

where $x(s_j)$ denotes the $x$ coordinate of a point $P_j$ with a curvilinear coordinate $s_j$ on the profile $j$, $j = 1, 2$, and $M_m$ are points located in the regions $V_m$. Another set of definitions for $\phi$ is written as

$$\phi_1^{-} = \left.\frac{\mathrm{d}F_0(x,y)}{\mathrm{d}\hat{n}_1}\right|_{s_1}\exp[-i\alpha_0 x(s_1)] \equiv \lim_{M_0\to P_1}\left[\frac{\mathrm{d}U_0(x,y)}{\mathrm{d}\hat{n}_1} + i\alpha_0 n_{1,x}U_0(x,y)\right], \quad (11a)$$

$$\phi_1^{+} = \left.\frac{\mathrm{d}F_1(x,y)}{\mathrm{d}\hat{n}_1}\right|_{s_1}\exp[-i\alpha_0 x(s_1)] \equiv \lim_{M_1\to P_1}\left[\frac{\mathrm{d}U_1(x,y)}{\mathrm{d}\hat{n}_1} + i\alpha_0 n_{1,x}U_1(x,y)\right], \quad (11b)$$

$$\phi_2^{-} = \left.\frac{\mathrm{d}F_1(x,y)}{\mathrm{d}\hat{n}_2}\right|_{s_2}\exp[-i\alpha_0 x(s_2)] \equiv \lim_{M_1\to P_2}\left[\frac{\mathrm{d}U_1(x,y)}{\mathrm{d}\hat{n}_2} + i\alpha_0 n_{2,x}U_1(x,y)\right], \quad (11c)$$

$$\phi_2^{+} = \left.\frac{\mathrm{d}[F_2(x,y) - F_i(x,y)]}{\mathrm{d}\hat{n}_2}\right|_{s_2}\exp[-i\alpha_0 x(s_2)] \equiv \lim_{M_2\to P_2}\left[\frac{\mathrm{d}U_2(x,y)}{\mathrm{d}\hat{n}_2} + i\alpha_0 n_{2,x}U_2(x,y)\right], \quad (11d)$$

where $\hat{n}_j$ denotes unit vectors normal to the $j$th profile at a point $P_j$, $j = 1, 2$.

It can be shown that, when the observation point $(x, y)$ is located on the profile, the right-hand sides of Eqs. (4)–(6) give the mean values of the expressions given by Eqs. (1), which are discontinuous. As a consequence,

$$U_0(s_1) = 1/2\left[\lim_{M_1\to P_1} U_0(x,y) + \lim_{M_0\to P_1} U_0(x,y)\right] = \frac{\psi_1^{-}(s_1)}{2}. \quad (12)$$

It has been taken into account that, according to Eqs. (1),

$$U_0(M_1) \equiv 0. \quad (13)$$

Then Eq. (4), when it is evaluated on $S_1$, gives

$$\frac{\psi_1^-(s_1)}{2} = -\int_{S_1} A_1^-(s_1, s_1')\phi_1^-(s_1')\mathrm{d}s_1' - \int_{S_1} B_1^-(s_1, s_1')\psi_1^-(s_1')\mathrm{d}s_1', \quad (14)$$

where $s_1$ is the couple $[x = x(s_1), y = y(s_1)]$ and a prime indicates another point on the same profile.

In a similar manner, Eq. (5) when it is evaluated on the lower profile gives a second equation for $\phi$ and $\psi$:

$$\frac{\psi_1^+(s_1)}{2} = \int_{S_1} A_1^+(s_1, s_1')\phi_1^+(s_1')\mathrm{d}s_1' + \int_{S_1} B_1^+(s_1, s_1')\psi_1^+(s_1')\mathrm{d}s_1' - \int_{S_1} \mathcal{A}_2^-(s_1, s_2')\phi_2^-(s_2')\mathrm{d}s_2' - \int_{S_1} \mathcal{B}_2^-(s_1, s_2')\psi_2^-(s_2')\mathrm{d}s_2'. \quad (15)$$

Here $s_2$ is the couple $[x = x(s_2), y = y(s_2)]$. A third equation also comes from Eq. (5) but is evaluated on the upper profile:

$$\frac{\psi_2^-(s_2)}{2} = \int_{S_1} \mathcal{A}_1^+(s_2, s_1')\phi_1^+(s_1')\mathrm{d}s_1' + \int_{S_1} \mathcal{B}_1^+(s_2, s_1')\psi_1^+(s_1')\mathrm{d}s_1' - \int_{S_1} A_2^-(s_2, s_2')\phi_2^-(s_2')\mathrm{d}s_2' - \int_{S_1} B_2^-(s_2, s_2')\psi_2^-(s_2')\mathrm{d}s_2'. \quad (16)$$

Equation (6) yields the fourth equation:

$$\frac{\psi_2^+(s_2)}{2} = \int_{S_2} A_2^+(s_2, s_2')\phi_2^+(s_2')\mathrm{d}s_2' + \int_{S_2} B_2^+(s_2, s_2')\psi_2^+(s_2')\mathrm{d}s_2'. \quad (17)$$

In Eqs. (14)–(17) the italic letters $A$ and $B$ stand for the kernels evaluated on one and the same profile, whereas script $\mathcal{A}$ and $\mathcal{B}$ denote kernels that depend on the coordinates of the two profiles.

In addition to Eqs. (14)–(17), the boundary conditions supply another set of four equations for the eight functions $\phi$ and $\psi$:

$$\psi_1^- = \psi_1^+, \quad (18)$$

$$\psi_2^- = \psi_2^+ + \psi_i, \quad (19)$$

$$q_1^-\phi_1^- = q_1^+\phi_1^+, \quad (20)$$

$$q_2^-\phi_2^- = q_2^+(\phi_2^+ + \phi_i), \quad (21)$$

with

$$q_1^- = \begin{cases} 1/\epsilon^{(0)} & \text{TM case} \\ 1/\mu^{(0)} & \text{TE case} \end{cases}, \quad (22)$$

$$q_1^+ = q_2^- = \begin{cases} 1/\epsilon^{(1)} & \text{TM case} \\ 1/\mu^{(1)} & \text{TE case} \end{cases}, \quad (23)$$

$$q_2^+ = \begin{cases} 1/\epsilon^{(2)} & \text{TM case} \\ 1/\mu^{(2)} & \text{TE case} \end{cases}, \quad (24)$$

and $\epsilon^{(j)}$ and $\mu^{(j)}$ are, respectively, the relative electric and magnetic permittivities of the $j$th media. According to Eq. (2),

$$\psi_i = \exp\left[-i\frac{2\pi}{\lambda}\nu_2\cos\theta_i y(s_2)\right],$$
$$\phi_i = -i\frac{2\pi}{\lambda}\nu_2\left[\frac{\mathrm{d}y(s_2)}{\mathrm{d}s_2}\sin\theta_i + \frac{\mathrm{d}x(s_2)}{\mathrm{d}s_2}\cos\theta_i\right] \times \exp\left[-i\frac{2\pi}{\lambda}\nu_2\cos\theta_i y(s_2)\right]. \quad (25)$$

Solving the system of eight equations (14)–(21) simultaneously enables us to find the unknown functions $\phi$ and $\psi$, which in turn we use to find the field everywhere in space, using Eqs. (4)–(6). For numerical implementation, however, solution of eight integral equations is too complicated, so in Section 3 we simplify them.

### 3. Numerical Formulation

Equations (18)–(21) make it easy to eliminate all $\phi^+$ and $\psi^+$. Equation (14) can be rewritten in the following form, which permits us to eliminate $\phi_1^-$:

$$\phi_1^- = C*\psi_1^-, \quad (26)$$

where $C$ is an integral operator applied over the function at its right and is composed of two operators:

$$C = -(A_1^-)^{-1}\left(B_1^- + \frac{I}{2}\right), \quad (27)$$

where $I$ is the identity operator and $A_1^-$ and $B_1^-$ are integral operators that denote an integration with kernels $A_1^-$ and $B_1^-$, respectively. $(A_1^-)^{-1}$ denotes an inverse operator of $A_1^-$. Using Eqs. (27) and similar notation, i.e., where an asterisk stands for inte-

gration of the corresponding kernel and the function, we can rewrite Eqs. (15) and (16) as

$$\mathcal{A}_2^{-}*\phi_2^{-} + \mathcal{B}_2^{-}*\psi_2^{-} = W_1*\psi_1^{-},$$
$$A_2^{-}*\phi_2^{-} + \left(B_2^{-} + \frac{I}{2}\right)*\psi_2^{-} = W_2*\psi_1^{-}, \qquad (28)$$

with

$$W_1 = B_1^{+} - \frac{I}{2} + \frac{q_1^{-}}{q_1^{+}} A_1^{+} C,$$
$$W_2 = \mathcal{B}_1^{+} + \frac{q_1^{-}}{q_1^{+}} \mathcal{A}_1^{+} C. \qquad (29)$$

Let us introduce a 2 by 2 matrix operator $Q$ such that

$$Q \equiv \begin{bmatrix} Q_{11} & Q_{12} \\ Q_{21} & Q_{22} \end{bmatrix} \overset{\text{def}}{=} \begin{bmatrix} \mathcal{A}_2^{-} & \mathcal{B}_2^{-} \\ A_2^{-} & B_2^{-} + I/2 \end{bmatrix}^{-1}; \qquad (30)$$

then Eqs. (28) permit us to eliminate both $\phi_2^{-}$ and $\psi_2^{-}$:

$$\begin{bmatrix} \phi_2^{-} \\ \psi_2^{-} \end{bmatrix} = \begin{bmatrix} R_1 \\ R_2 \end{bmatrix} * \psi_1^{-}, \qquad (31)$$

where

$$\begin{bmatrix} R_1 \\ R_2 \end{bmatrix} = Q \begin{bmatrix} W_1 \\ W_2 \end{bmatrix}. \qquad (32)$$

Finally, Eq. (17) enables us to determine the single unknown function $\psi_1^{-}$:

$$\left[\frac{q_2^{-}}{q_2^{+}} A_2^{+} R_1 + \left(B_2^{+} - \frac{I}{2}\right) R_2\right] * \psi_1^{-} = A_2^{+} * \phi_i + \left(B_2^{+} - \frac{I}{2}\right) * \psi_i. \qquad (33)$$

To enable the integral operators to be applied to unknown functions, the formulation of the integral method proposed in Ref. 11 uses the trapezoidal rule, with special attention paid to the singularities of the kernels. Then the integral operators are replaced by matrix multiplication in the following manner: The unknown functions $\phi_j$ and $\psi_j$ are projected onto the set of points on the profiles $P_{j,p}$, $j = 1, 2$ and $p = 1, \ldots N_p$, so the unknown functions are replaced by unknown column vectors ${\phi_{j,p}}^{\pm}$ and ${\psi_{j,p}}^{\pm}$. The integral operators are replaced by matrix multiplication, and the kernels by square matrices:

$$A_{j,pq}^{\pm} = 1/2\, A_j^{\pm}[s_j(P_{j,p}), s_j(P_{j,q})][s_j(P_{j,q+1}) - s_j(P_{j,q-1})], \qquad p \neq q,$$
$$\mathcal{A}_{j,pq}^{\pm} = 1/2\, \mathcal{A}_j^{\pm}[s_i(P_{i,p}), s_j(P_{j,q})][s_i(P_{i,q+1}) - s_j(P_{j,q-1})], \qquad i \neq j, \qquad (34)$$

and similar expressions for $B$ and $\mathcal{B}$. The diagonal terms of $A$ and $B$ exhibit singularities that can be integrated in closed form, as explained in detail in Ref. 11. Then Eqs. (26)–(33) represent standard matrix operations in which the inverse integral operators in Eqs. (27) and (30) are replaced by matrix inversion. Equation (33) becomes a linear algebraic equation for the unknown vector ${\psi_{1,p}}^{-} \equiv {\psi_1}^{-}(s_{1,p})$, $s_{1,p} = s_1(P_{1,p})$ with the substitution ${\phi_{i,p}} \equiv \phi_i(s_{2,p})$, ${\psi_{i,p}} \equiv \psi_i(s_{2,p})$, where $s_{2,p} = s_2(P_{2,p})$. Once ${\psi_{1,p}}^{-}$ are determined, ${\psi_{2,p}}^{-}$ and ${\phi_{2,p}}^{-}$ are calculated from Eq. (31). The unknown values of ${\phi_{1,p}}^{-}$ are determined from Eq. (26), and all the functions with upper index (+) are easily found from the boundary conditions, Eqs. (18)–(21).

We can obtain the diffraction efficiencies in the reflected orders propagating above the grating by representing $U_2$ in the form of a Rayleigh expansion, which is always valid above the top of the grooves of the upper profile:

$$U_2(x, y) = \sum_{m=-\infty}^{\infty} r_n \exp(inKx + i{\beta_{2,m}}^{+} y). \qquad (35)$$

When we compare Eq. (35) with Eq. (6) and take into account the form of kernels given in Eqs. (7) and (8) with $y \geq y_2(s_2)$, we can easily conclude that the amplitudes of the reflected orders $r_m$ are equal to

$$r_m = \frac{1}{2id{\beta_{2,m}}^{+}} \int_{S_2} \exp[-\mathrm{Im}\, Kx_2(s_2) - i{\beta_{2,m}}^{+} y_j(s_j)]{\phi_2}^{+}(s_2)\mathrm{d}s_2 + \frac{1}{2d} \int_{S_2} \left(\frac{\mathrm{d}x_2}{\mathrm{d}s_2} - \frac{\alpha_m}{{\beta_{2,m}}^{+}} \frac{\mathrm{d}y_2}{\mathrm{d}s_2}\right) \exp[-\mathrm{Im}\, Kx_2(s_2) - i{\beta_{2,m}}^{+} y_j(s_j)]{\psi_2}^{+}(s_2)\mathrm{d}s_2. \qquad (36)$$

The diffraction efficiencies are determined from the well-known relation

$$\eta_m = \frac{{\beta_{2,m}}^{+}}{{\beta_{2,0}}^{+}} |r_m|^2. \qquad (37)$$

If necessary, the transmission efficiencies can be found in a similar manner.

#### 4. Test of Validity and Numerical Problems

We implemented the theoretical approach presented in Sections 2 and 3 numerically, using the existing numerical code for bare echelles. We used classic tests with the energy balance criterion for a lossless dielectric or a perfectly conducting substrate, a reciprocity theorem, and convergence testing to check the validity of the theory and the code. In addition, when the overcoating had an optical index equal to that of the substrate or the superstrate, we carried out a test against the results for a bare grating. For a sinusoidal grating the results of the code coincided with the results obtained by the method of Chandezon *et al.*,[8] as we show at the end of Section 5.

The main numerical problems arise in two extreme cases:

(i) Wavelength $\lambda$ much larger than layer thickness $t$. Here the profiles are situated too close to each

other, compared to λ, so kernels $\mathcal{A}$ and $\mathcal{B}$ become large in modulus for $s_2 \to s_1$. This behavior has the same origin as the singularities of kernels A and B (Ref. 11) and can be eliminated in the same manner. However, we have not done so yet because we are interested in the absorption in the spectral region near 100 nm, where a typical layer thickness of approximately 5–25 nm causes no problems.

(ii) Period $d$ much longer than layer thickness $t$. If the wavelength is not too much larger than $t$, the kernels have no singularities, but their moduli have maxima when the distance $|P_{2,p}P_{1,q}|$ between two points located upon the two different profiles is small. The width of these maxima is of the order of magnitude of the layer thickness; thus the correct application of the trapezoidal integration rule requires that the distance between two consecutive points of the profile discretization $\Delta = |s_{j,p} - s_{j,p-1}|$ be less than the width of the maxima. When, roughly, $\Delta \approx d/N_p$, where $N_p$ is the number of integration points, then the lower limit of $N_p$ is determined by the relation

$$N_{p,\min} \propto d/t. \tag{38}$$

Thus values of $d$ of ~10 μm and of $t$ of 20 nm require that the number of integration points exceed 500. Note that $N_p$ directly determines the number of unknown values of $\phi_{j,m}$ and $\psi_{j,m}$ and thus the size of the matrices to be used. Practically, it is not worthwhile for $N_p$ to exceed 1000, because of the computation time, memory requirements, roundoff errors, and limited computer word length that would be involved. In such a case it would be necessary to find another way to integrate the product of the unknown functions and the kernels rather than using the trapezoidal rule. The numerical results presented in Section 5 were obtained for $N_p$ as large as 600, which is sufficient for treating echelles that have more than 100 grooves per millimeter. However, if an analysis of echelles with larger periods is required, it is better to develop another way to perform the integration.

### 5. Diffraction Efficiency of Echelles Covered with Aluminum Oxide or Magnesium Fluoride in the Spectral Region 70–190 nm

It is well known that below 160 nm the reflectivity (and thus the efficiency) of aluminum gratings degrades because of the edge absorption of the oxide layer that naturally forms upon a surface exposed to air. For this absorption to be prevented, sometimes magnesium fluoride can be deposited onto the surface immediately after the grating replication to prevent the aluminum from oxidizing. Also, the absorption of $MgF_2$ increases below 110 nm, thus limiting its applications. Below 110 nm, other reflecting materials are used, more or less successfully.[23]

Figure 2 is a schematic of an echelle with an 80° groove angle and the incident wave perpendicular to the small facet. Only a few of the numerous diffracted orders are shown, and typically high efficiency is expected in the orders with direction of propagation almost opposite the incident wave. The

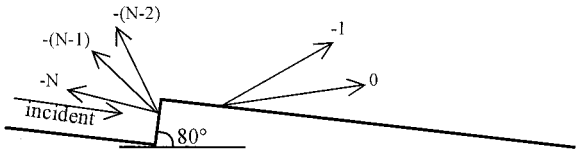


Fig. 2. Schematic representation of a reflective echelle. Only a few diffracted orders are shown.

numerical results for the total reflectivity are given in Fig. 3 for an echelle with 83 grooves/mm and an 80° groove angle. By total reflectivity we mean the sum of efficiencies of all reflected diffraction orders where the remaining part to unity are absorbed in the layer and in the substrate. The two fundamental polarizations are shown by solid (TE) and dashed (TM)

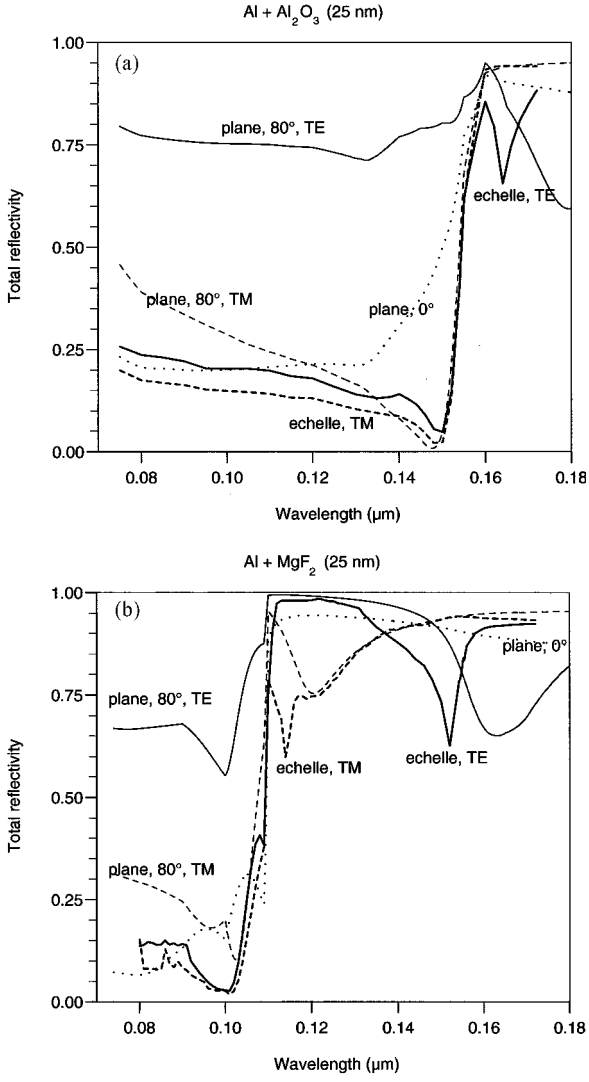


Fig. 3. Total reflectivity of an aluminum surface covered by 25-nm-thick layers of $Al_2O_3$ or $MgF_2$ as a function of wavelength. Solid curves, TE polarization; dashed curves, TM polarization; thinner curves, plane mirror at an 80° angle of incidence; heavier curves, echelle with 83 grooves/mm, 80° groove angle, and incidence of 80°; dotted curves, normal incidence upon a plane mirror.

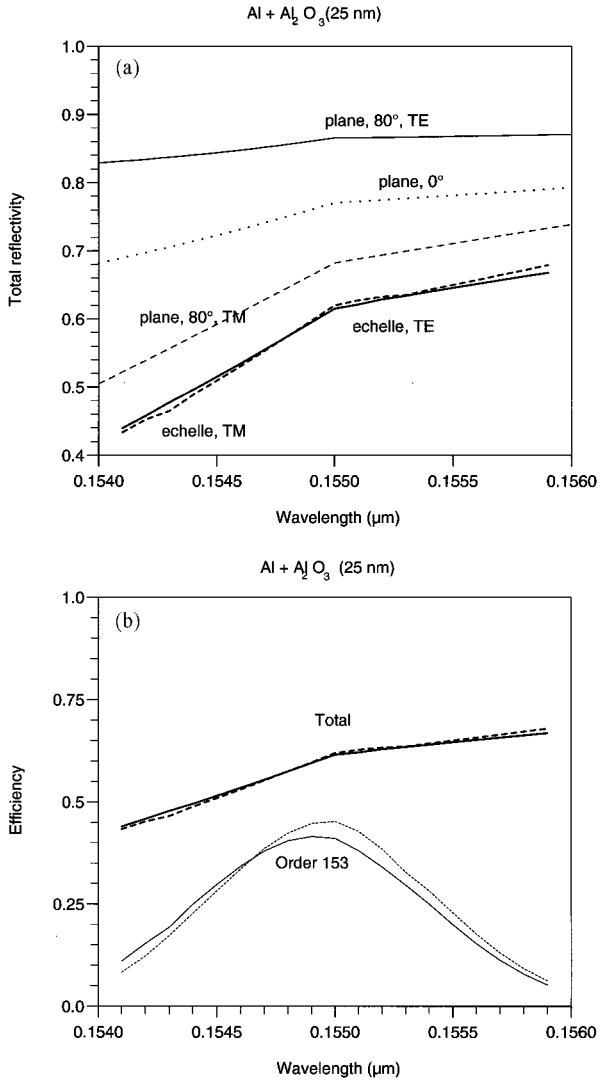


Fig. 4. (a) Detailed view of Fig. 3(a) in the vicinity of the absorption edge of $Al_2O_3$. (b) Diffraction efficiency (thinner curves) in order 153 and the total diffracted energy (heavier curves) of the echelle described in Fig. 3.

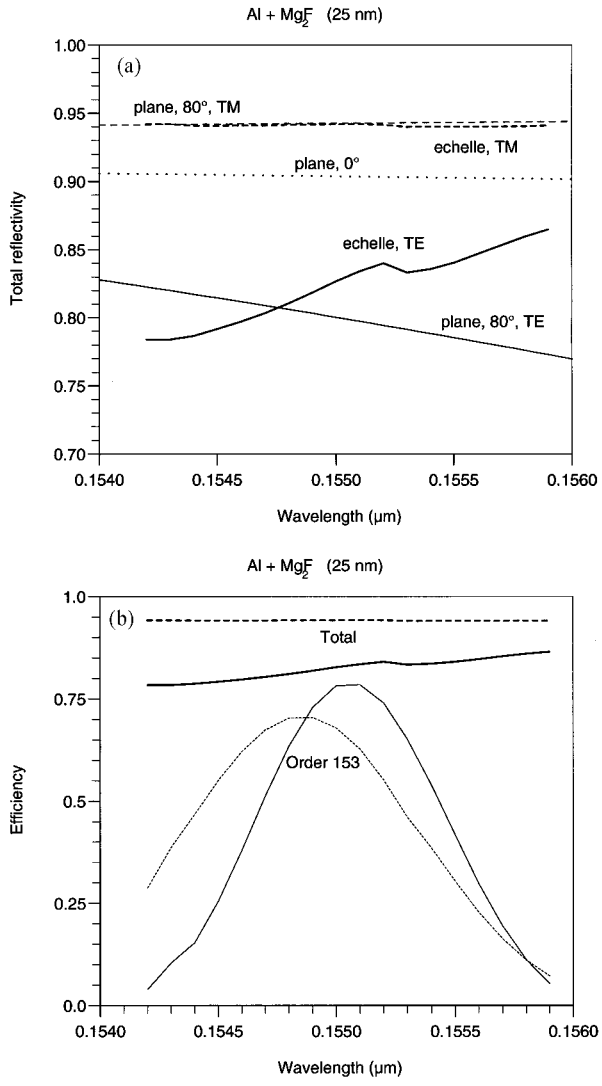


Fig. 5. Same as in Fig. 4 but for a $MgF_2$ covering layer.

curves. For comparison, the reflectivities of the plane aluminum mirrors covered with the same layers are given, both at the same angle of incidence ($\theta_i$ = 80°; thinner curves) and at normal incidence; the dotted curve stands for both polarizations. The high reflectivity of the plane surface below the absorption edge in TE polarization at 80° incidence has no effect on raising the grating reflectivity because the incident light hits the small (working) facet perpendicularly.

It can be concluded that the grating reflectivity follows the worst possible course, its reflectivity keeping low values below the absorption edge. Above the absorption edge in both TE and TM polarization there is an anomaly for a MgF2 coating and a similar one in TE polarization for the oxide layer, which probably is due to the presence of some resonances inside the dielectric layers, of either the guided-wave or the Fabry–Perot type, because the wavelength is of the same order of magnitude as the optical layer thickness.

Another peculiarity is that the minimum at the lower side of the absorption edge is much lower than the corresponding plane-mirror reflectivity, in both TE and TM polarization following the minimum observed for the plane-mirror reflectivity in TM polarization at an incidence of 80°.

Figures 4 and 5 present more-detailed views in the vicinity of the oxide absorption edge, including the efficiencies in the blazing order, the 153rd for these values of $d$ and $\lambda$. It is obvious [Fig. 4(a)] that the reflectivity of the grating covered with $Al_2O_3$ is less that the reflectivity of the plane mirror for both polarizations; the diffraction efficiency does not exceed 45% [Fig. 4(b)]. A coating of $MgF_2$ results in a diffraction efficiency of ~75%, depending on the polarization [Fig. 5(b)]. The total reflectivity in TM polarization is the same for the grating and the plane mirror, whereas the TE grating reflectivity partially exceeds the reflectivity of the plane mirror for the same incidence.

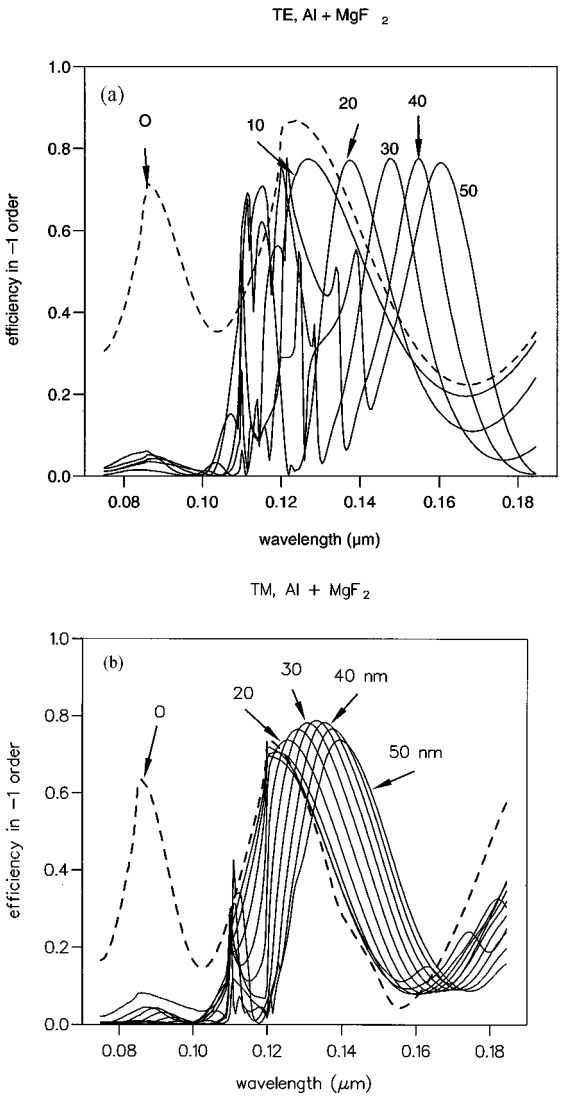


Fig. 6. Spectral dependence of diffraction efficiency in order −1 of an aluminum sinusoidal grating with period $d = 0.3$ μm and groove depth $h = 0.12$ μm in a −1-order Littrow mount. The grating is covered with layers of $MgF_2$ with the thicknesses (in nanometers) shown. (a) TE polarization, (b) TM polarization. Dashed curves, bare aluminum grating.

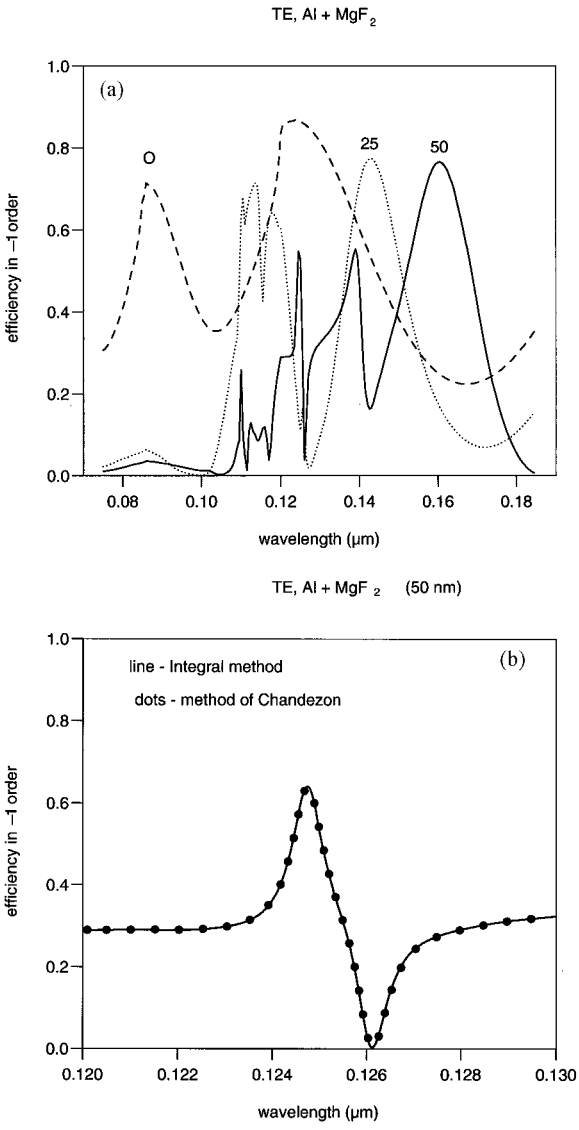


Fig. 7. (a) Same as in Fig. 6(a), but here only three layer thicknesses are presented to permit the anomalies in the spectral region 0.10–0.12 μm to be seen. (b) Comparison of the results of the integral method and the formalism of Chandezon *et al.*[8] for the sinusoidal grating presented in Fig. 6 for a layer 50 nm thick.

## 6. Performance of a Sinusoidal Grating

There is a long history of comparing blazed and holographic gratings. Usually it is considered that sinusoidal gratings are limited in applications when high efficiency in unpolarized light is required, as it is for spectroscopic measurements. This requirement is stronger in astronomy, for which exposition time is the leading cost determinant.

Figure 6 shows that even in this spectral range sinusoidal gratings can have high efficiency in unpolarized light, i.e., simultaneously blazing in TE and TM polarizations. Of course, unlike for echelles, this blazing does not switch to different orders when blazing is required in the minima of a given order, which is inconvenient for astronomy. In addition, the angular dispersion of the grating in a Littrow mount is $(2/\lambda)\tan\theta_i$ and does not depend on the groove frequency, so the angular dispersion of the echelle considered in Section 4 will be 75 $\mu m^{-1}$, 22 times greater than the value of 3.4 μm for the sinusoidal grating with 3333 grooves/mm presented here.

It can be observed that by varying the thickness of the covering layer one can tune the spectral position of the maximum efficiency in a spectral interval equal to the maximum width. The peak at 85 nm is due to the fact that with null thickness the absorption corresponds to the absorption of bare (without oxide) aluminum, whose absorption edge lies at shorter wavelengths; but once exposed to air this peak gradually decreases with time because of the formation of an oxide layer.

Figure 7(a) shows only three curves of those shown in Fig. 6(a) so we can distinguish their behavior below the maxima, which is practically impossible from Fig.

6(a). A formation of narrow and sharp anomalies can be observed, which is typical for guided-wave excitation. One of these anomalies is enlarged in Fig. 7(b) to show a comparison between the results of the newly developed theoretical method and the method of Chandezon *et al.*,[8] which works quite well for sinusoidal gratings.

## 7. Conclusion

A generalization of the integral method to gratings covered with dielectric layers (lossless or absorbing) has been presented, based on solution of a set of coupled integral equations. A numerical study was presented of an aluminum echelle in the vicinity of the absorption edges of $Al_2O_3$ and of $MgF_2$. It was shown that the details of the total reflectivity (and thus of efficiency) behavior differ from the reflectivity of the corresponding flat mirror. A sinusoidal grating can have similar performance in TE and TM polarization with the possibility of tuning the spectral position of the efficiency maximum by varying the thickness of the $MgF_2$ layer.

E. Popov and B. Bozhkov acknowledge the help of the Ministry of Education and Science of Bulgaria under contract 714 with the National Science Foundation of Bulgaria.

## References and Note

1. M. Nevière, G. Cerutti-Maori, and M. Cadilhac, "Sur une nouvelle méthode de résolution du problème de la diffraction d'une onde plane par un réseau infiniment conducteur," Opt. Commun. **3,** 48–52 (1971).
2. L. Li, "Formulation and comparison of two recursive matrix algorithms for modeling layered diffraction gratings," J. Opt. Soc. Am. A **13,** 1024–1035 (1996).
3. F. Montiel and M. Nevière, "Differential theory of gratings: extension to deep gratings of arbitrary profile and permittivity via the *R*-matrix propagation algorithm," J. Opt. Soc. Am. A **12,** 2672–2678 (1995).
4. M. G. Moharam and T. K. Gaylord, "Diffraction analysis of dielectric surface-relief gratings," J. Opt. Soc. Am. **72,** 1385–1392 (1982).
5. L. Li, "Multilayer modal method for diffraction gratings of arbitrary profile, depth, and permittivity," J. Opt. Soc. Am. A **10,** 2581–2591 (1993).
6. P. Lalanne and G. Morris, "Highly improved convergence of the coupled-wave method for TM polarization," J. Opt. Soc. Am. A **13,** 779–784 (1996).
7. G. Granet and B. Guizal, "Efficient implementation of the coupled-wave method for metallic lamellar gratings in TM polarization," J. Opt. Soc. Am. A **13,** 1019–1023 (1996).
8. J. Chandezon, M. T. Dupuis, G. Cornet, and D. Maystre, "Multicoated gratings: a differential formalism applicable in the entire optical region," J. Opt. Soc. Am. **72,** 839–846 (1982).
9. J. P. Plumey, B. Guizal, and J. Chandezon, "The coordinate transformation method as applied to asymmetric gratings with vertical facets," J. Opt. Soc. Am. A **14,** 610–617 (1997).
10. G. Granet, J. Chandezon, and O. Coudert, "Extension of the C method to nonhomogeneous media: application to nonhomogeneous layers with parallel modulated faces and to inclined lamellar gratings," J. Opt. Soc. Am. A **14,** 1576–1582 (1997).
11. D. Maystre, "Integral method," in *Electromagnetic Theory of Gratings*, R. Petit, ed. (Springer-Verlag, Berlin, 1980), Chap. 3.
12. E. Loewen, D. Maystre, E. Popov, and L. Tsonev, "Echelles: scalar, electromagnetic, and real-groove properties," Appl. Opt. **34,** 1707–1727 (1995).
13. E. Loewen, D. Maystre, E. Popov, and L. Tsonev, "Diffraction efficiency of echelles working in extremely high orders," Appl. Opt. **35,** 1700–1704 (1996).
14. D. Maystre, "A new general integral theory for dielectric coated gratings," J. Opt. Soc. Am. **68,** 490–495 (1978).
15. D. Maystre, "A new theory for multiprofile, buried gratings," Opt. Commun. **26,** 127–132 (1978).
16. A. Pomp, "The integral method for coated gratings: computational cost," J. Mod. Opt. **38,** 109–120 (1991).
17. D. Maystre, "Electromagnetic study of photonic band gaps," Pure Appl. Opt. **3,** 975–993 (1994).
18. Lord Rayleigh, "On the dynamical theory of gratings," Proc. R. Soc. London Ser. A **79,** 399–416 (1907).
19. R. F. Millar, "The Rayleigh hypothesis and a related least-squares solution to scattering problems for periodic surfaces and other scatterers," Radio Sci. **8,** 785–796 (1973); M. Nevière and M. Cadilhac, "Sur la validite du developpement de Rayleigh," Opt. Commun. **2,** 235–238 (1970).
20. A. Wirgin, "Sur la théorie de Rayleigh de la diffraction d'une onde par une surface sinusoidale," C. R. Acad. Sci. Ser. B **288,** 179–182 (1979).
21. E. Popov and L. Mashev, "Convergence of Rayleigh Fourier method and rigorous differential method for relief diffraction gratings: nonsinusoidal profile," J. Mod. Opt. **34,** 155–158 (1987).
22. P. M. Van den Berg, "Reflection by a grating: Rayleigh methods," J. Opt. Soc. Am. **71,** 1224–1229 (1981).
23. See E. Loewen and E. Popov, *Diffraction Gratings and Applications* (Marcel Dekker, New York, 1997), Chap. 4.